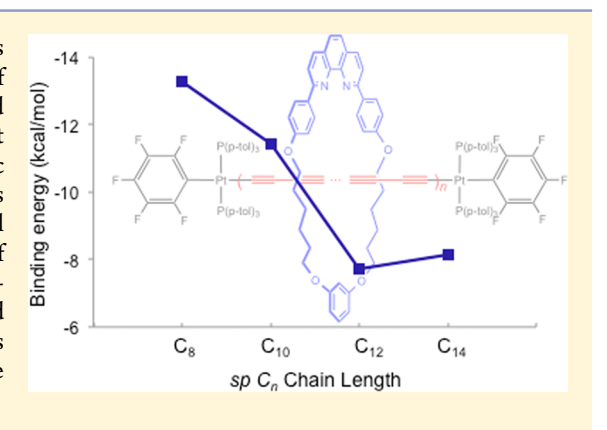
A Metal-Capped Conjugated Polyyne Threaded through a Phenanthroline-Based Macrocycle. Probing beyond the Mechanical Bond to Interactions in Interlocked Molecular Architectures

Hiba Sahnoune,[†] Zuzana Baranová,[‡] Nattamai Bhuvanesh,[‡] John A. Gladysz,*,[‡] and Jean-François Halet*,†

Supporting Information

ABSTRACT: DFT calculations with long-range dispersion corrections have been used to analyze the structures and binding energies of rotaxanes featuring dimetal polyynediyl Pt₂C_n dumbbells threaded through a 1,10-phenanthroline-based macrocycle. Results indicate that (i) the threading of the organometallic wire hardly affects its geometric and electronic properties and (ii) the noncovalent binding energies between the axle and macrocycle not only arise from mechanical bonding enforced weak interactions derived from the close proximity of the sp carbon chain to the macrocycle atoms, but also include hydrogenbonding contacts involving hydrogen atoms of the metal bound phosphine ligands of the former and the nitrogen and oxygen atoms of the latter. The optimized geometries of the rotaxane and macrocycle are compared to the corresponding crystal structures where available.



INTRODUCTION

Bimetallic complexes with π -conjugated carbon bridges¹ are often referred to as molecular wires² and have attracted great attention because of their potential applications in molecular electronics.³ In these compounds, the carbon chain length represents one of the several fundamental structural variables, and various redox-active bimetallic polyynediyl complexes $L_mM(C \equiv C)_nML_m$ containing carbon chains that can be extended to over 20 atoms are well documented.⁴ However, previous studies have clearly shown that the lengthening of the polyynediyl linkers is sometimes limited by their poor chemical stability due to linker-solvent and/or linker-linker reactions.⁵ Introduction of aromatic rings or even organometallic units in the polyynediyl spacer constitutes an attractive strategy to circumvent this instability and eventually to tune their physical properties. 1,6 An alternative way to prevent interchain crosstalk, which would also alter the optical and electronic properties of these assemblies, is to insulate the unsaturated carbon linkers.⁷ One of us has prepared a series of diplatinum polyynediyl complexes insulated by $\alpha_i \omega$ -polymethylene diphosphine ligands that bridge from one organometallic end group to the other.8 This approach to insulated double-helical "beanpole" molecular wires (IMWs) is quite unique in that it relies only on van der Waals interactions between the wrapped polyynyl and the enveloping polymethylene chains. Another strategy to prepare IMWs consists of stabilizing polyyne "axles" by threading them through macrocyclic "beads" to form

Recently, the second approach was successfully realized through the synthesis of a [2]rotaxane featuring a dimetal polyynediyl axle threaded through a phenanthroline-based macrocycle, namely $[trans, trans-(C_6F_5)(p-tol_3P)_2Pt(C \equiv$ $C)_4Pt(P-p-tol_3)_2(C_6F_5)]\subset (2,9-(1,10-phenanthrolinediyl))(p-$ C₆H₄O(CH₂)₆O)₂(1,3-C₆H₄), or **2·3** (Figure 1). Similarly, a C₁₂ rotaxane of macrocycle 3 with bulky organic end groups, $[(3,5-t-Bu_2C_6H_3)_3C(C \equiv C)_6C(3,5-t-Bu_2C_6H_3)_3] \subset (2,9-(1,10-t)^2C_6H_3)_3$ phenanthrolinediyl)) $(p-C_6H_4O(CH_2)_6O)_2(1,3-C_6H_4)$, has been characterized. 10 The axles and beads in rotaxanes are considered to be joined by mechanical bonds. 11 Accordingly, we sought to investigate the nature of the bonding interactions between the two components in the bimetallic system, the axle or Pt₂C₈ "dumbbell" 2 and bead or macrocycle 3.

In this paper, we analyze theoretical results obtained at the density functional theory (DFT) level to provide some insight regarding noncovalent electronic interactions 12 between the rotaxane components in the interlocked system 2.3 as well as (still) hypothetical higher homologues. The crystal structure of macrocycle 3, which has not previously been reported, is also detailed and compared to those described earlier for 2¹³ and 2. 3.9 All of these structures are contrasted with the respective computed geometries.

Received: July 18, 2013 Published: October 24, 2013

[†]Institut des Sciences Chimiques de Rennes, UMR 6226, CNRS-Université de Rennes 1, F-35042 Rennes, France

[‡]Department of Chemistry, Texas A&M University, P.O. Box 30012, College Station, Texas 77842-3012, United States

$$F = \begin{cases} F \\ P(p-tol)_3 \\ Pt \\ P(p-tol)_3 \end{cases}$$

$$F = \begin{cases} P(p-tol)_3 \\ P(p-tol)_3 \\ F \end{cases}$$

$$F = \begin{cases} P(p-tol)_3 \\ P(p-tol)_3 \\ P \end{cases}$$

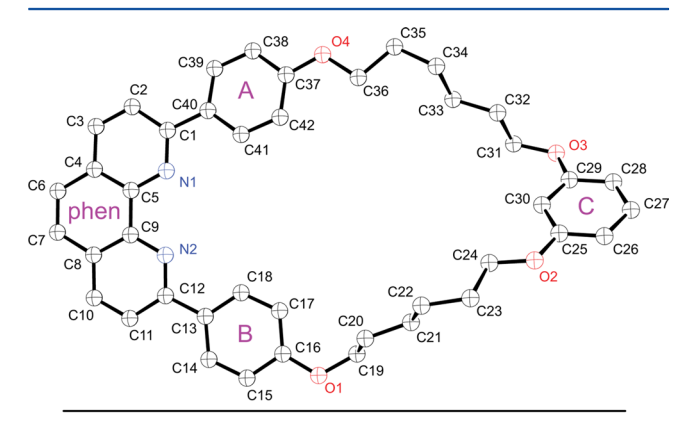
$$F = \begin{cases} P(p-tol)_3 \\ P(p-tol)_3 \\ P \end{cases}$$

Figure 1. Representation of rotaxane 2.3.

RESULTS AND DISCUSSION

1. Geometries of Rotaxanes and their Components.

The components of the rotaxane **2·3** were first optimized and analyzed separately and then together. The minimum energy structure for the macrocycle **3** is given in Figure 2 (top), and that for **2·3** is provided in Figure 3 (top). The structures of reasonably close models for the axle **2**, trans,trans- (C_6F_5) - $(H_3P)_2Pt(C\equiv C)_nPt(PH_3)_2(C_6F_5)$] $(n = 2-6, 8, 10, 12)^{14}$ have been computed earlier; therefore, the rather similar geometry found for **2** is not depicted.



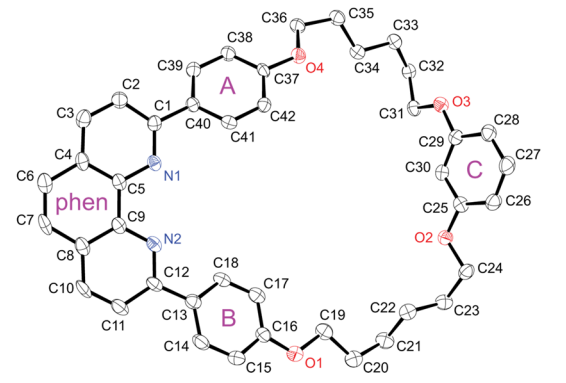
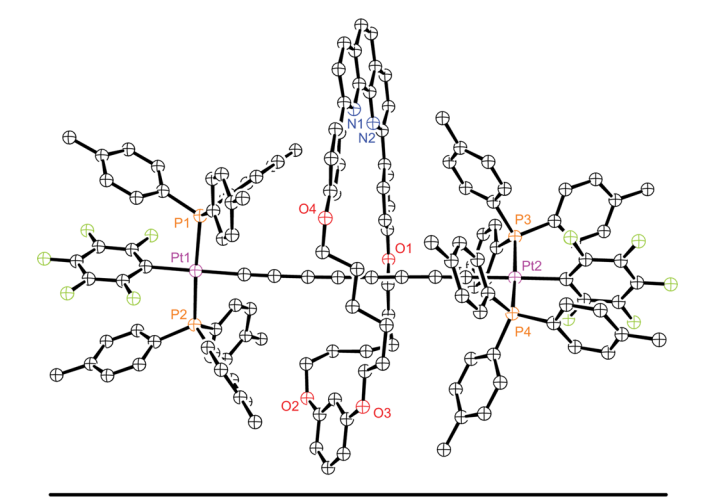


Figure 2. Structure of **3** obtained from DFT calculations (top) and the X-ray crystal structure with thermal ellipsoids at the 50% probability level (bottom). Hydrogen atoms are omitted for clarity.



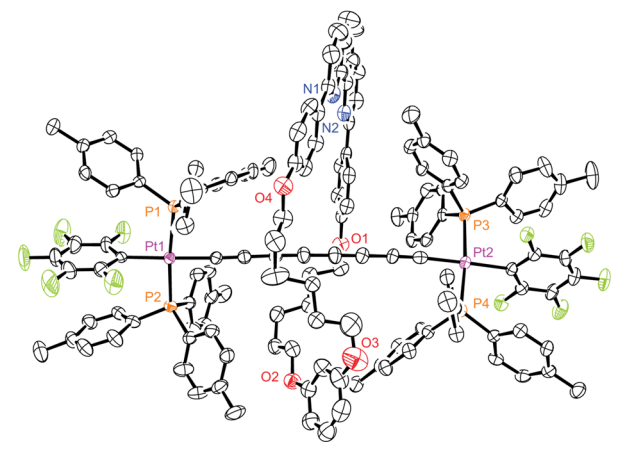


Figure 3. Structure of 2·3 obtained from DFT calculations (top) and the X-ray crystal structure with thermal ellipsoids at the 50% probability level (bottom). Hydrogen atoms are omitted for clarity.

The crystal structure of **3** was determined as part of this study as described in the Experimental Section and Supporting Information (Table S1). Those of **2** and **2**·**3** have been previously reported. The molecular structure of **3** is depicted in Figure 2 (bottom), and selected experimental and computational data are compared in Table 1 and in Table S2 (Supporting Information).

For the axle 2, the bead 3, and the rotaxane $2\cdot3$, the optimized distances compare rather well with the experimental data (Tables 1 and Table S2 (Supporting Information)). In $2\cdot3$, for instance, the computed Pt–C distances (2.004 and 2.005 Å) are quite close to the experimental values (1.993(3) and 1.990(5) Å). The optimized C–C bond lengths also match fairly well with experiment, with the largest discrepancy being 0.016 Å. As observed in earlier work, ¹⁴ the Pt–P bond lengths in 2 and $2\cdot3$ are overestimated by ca. 0.05 Å. In any case, the bond lengths and angles associated with the PtC₈Pt dumbbell axle do not change much upon threading with 3. For example, the computed Pt1–C1 and C1 \equiv C2 distances increase by only 0.005 and 0.002 Å, respectively.

The geometry of the macrocycle 3 can be analyzed with respect to that of 2·3. First, consider the computed structure as compared to that found in the crystal structure (Figure 2, top and bottom). The latter is, of course, affected by crystal-packing forces, whereas the former represents the gas-phase energy minimum. Interestingly, neither structure exhibits any non-trivial symmetry element. The least-squares planes of p-C₆H₄O

du det een (10.1001 /een 100700 e.l. Oen een ekstilten 2012, 20. caca. caca.

Table 1. Selected Computed Bond Lengths (Å) for 2, 2^+ , and $2 \cdot 3^a$

2	2+	2.3
1.999 [1.951(5)]	1.959	2.004 [1.993(3)]
1.245 [1.252(6)]	1.264	1.247 [1.207(5)]
1.361 [1.365(6)]	1.330	1.362 [1.358(6)]
1.242 [1.209(6)]	1.261	1.244 [1.206(7)]
1.354 [1.351(8)]	1.323	1.356 [1.359(7)]
1.242 [1.209(6)]	1.261	1.244 [1.213(6)]
1.361 [1.365(6)]	1.330	1.362 [1.346(5)]
1.245 [1.252(6)]	1.264	1.247 [1.213(6)]
1.999 [1.951(5)]	1.958	2.005 [1.990(5)]
2.085 [2.059(4)]	2.077	2.081 [2.071(3)]
2.351 [2.299(1)]	2.373	2.348 [2.299(1)]
2.355 [2.306(1)]	2.373	2.362 [2.306(1)]
2.083 [2.059(4)]	2.079	2.083 [2.080(4)]
2.352 [2.297(1)]	2.372	2.352 [2.297(1)]
2.352 [2.305(1)]	2.372	2.351 [2.305(1)]
1.359 [1.360]	1.328	1.360 [1.354]
1.243 [1.231]	1.262	1.245 [1.210]
13.048 [12.895(3)]	12.949	13.062 [12.839(7)]
	1.999 [1.951(5)] 1.245 [1.252(6)] 1.361 [1.365(6)] 1.242 [1.209(6)] 1.354 [1.351(8)] 1.242 [1.209(6)] 1.361 [1.365(6)] 1.245 [1.252(6)] 1.999 [1.951(5)] 2.085 [2.059(4)] 2.351 [2.299(1)] 2.355 [2.306(1)] 2.083 [2.059(4)] 2.352 [2.297(1)] 2.352 [2.305(1)] 1.359 [1.360] 1.243 [1.231]	1.999 [1.951(5)] 1.959 1.245 [1.252(6)] 1.264 1.361 [1.365(6)] 1.330 1.242 [1.209(6)] 1.261 1.354 [1.351(8)] 1.323 1.242 [1.209(6)] 1.261 1.361 [1.365(6)] 1.330 1.245 [1.252(6)] 1.264 1.999 [1.951(5)] 1.958 2.085 [2.059(4)] 2.077 2.351 [2.299(1)] 2.373 2.083 [2.059(4)] 2.079 2.352 [2.297(1)] 2.372 2.352 [2.305(1)] 2.372 1.359 [1.360] 1.328 1.243 [1.231] 1.262

^aExperimental crystallographic data are given in brackets.

rings (see A and B in Figure 2) in the crystal are somewhat more twisted with respect to the least-squares plane of the phenanthroline moiety than in the computed structure (30.4 and 19.0° vs 8.8 and 6.7°; Table S2 (Supporting Information)). These values are closely mirrored by the corresponding N– $C_{\rm phen}$ – $C_{\rm aryl}$ – $C_{\rm aryl}$ torsion angles (Table S2).

As is obvious in Figure 2, the conformations of the sp³ carbon segments differ significantly. The four atom linkages that run from O4 to O3 exhibit gauche, anti, anti, gauche, and gauche conformations in the crystal, but anti, gauche, anti, anti, and anti conformations in the computed structure, as reflected by the torsion angles. For the linkages that run from O1 to O2, the corresponding conformations are anti, gauche, anti, anti, and gauche and then anti, anti, anti, gauche, and anti, respectively. However, the bond lengths and bond angles closely correspond, with differences less than 0.02 Å and 2.0°, respectively. The former are summarized in Table S2 (Supporting Information).

Analogous to the findings with the PtC₈Pt axle above, the bond lengths and angles associated with the macrocycle bead in 2·3 are similar to those computed for free 3 (Table S2 (Supporting Information)). The bond lengths exhibit a maximum deviation of 0.02 Å. However, the least-squares planes of the p-C₆H₄O rings with respect to that of the phenanthroline moiety are 8.2 and 21.1°, respectively, reflecting a somewhat altered conformation. The four atom linkages that run from O4 to O3 exhibit anti, gauche, anti, anti, and anti conformations in the crystal but anti, anti, anti, gauche, and anti conformations in the computed structure. For the linkages that run from O1 to O2, the corresponding conformations are anti, anti, anti, gauche, and anti and then anti, gauche, gauche, anti, and gauche, respectively. Both patterns in the crystal of 2·3 agree with the O4 to O3 and O1 to O2 segments in computed

In accord with experimental structural findings with both 2 and 2·3, as well as a host of related diplatinum polyynediyl complexes, 8,13 $\pi \cdots \pi$ aromatic stacking interactions between the C_6F_5 groups and tolyl groups of the p-tol₃P ligands are computed. As summarized in Table S3 (Supporting Informa-

tion), the calculated and experimental stacking distances and angles for $2\cdot3$ (defined per the table) are 3.886 vs 3.847 Å and 157 vs 154°, respectively. Also, the proximity of the sp carbon chain to various macrocycle atoms can be compared. The computed average ($C(\text{sp-chain})-C(\text{sp}^3\text{-macrocycle})$ distance is 4.576 Å, slightly longer than the average experimental value of 4.207 Å (see Table S3). The $C(\text{sp}^2\text{-macrocycle})$ distances are much more remote (5.991 vs 6.081 Å).

In addition, the computations show that some weak hydrogen bonds (in the range of 2.50–3.10 Å), derived from the $\rm C_6H_4$ and $\rm CH_3$ hydrogen atoms of the tri-p-tolylphosphine ligands tethered to the platinum centers and the oxygen and nitrogen atoms of the macrocycle, are present. These individually weak interactions between the thread and the bead are computed to be collectively attractive by $-13.27~\rm kcal/mol$. This point will be further analyzed later on.

2. MO Diagrams. The molecular orbital (MO) diagrams of the rotaxane 2·3 and its components 2 and 3 are shown in Figure 4. As noted above, a model for 2, trans,trans-

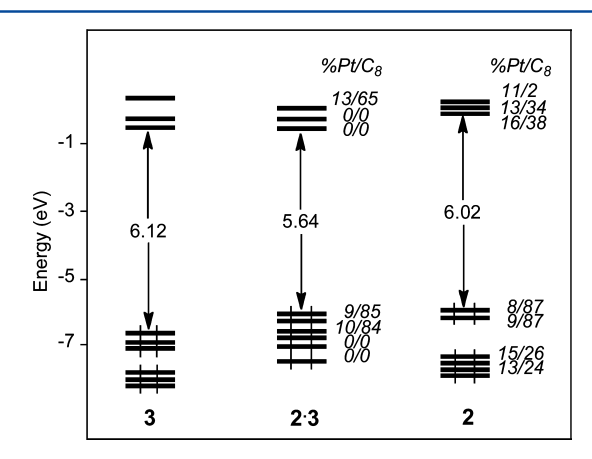


Figure 4. DFT molecular orbital diagrams of 2·3 (center) and the components 2 (right) and 3 (left). The relative Pt/carbon chain percentage contributions are given in italics.

[(C_6H_5)(H_3P)₂Pt($C \equiv C$)₄Pt(PH_3)₂(C_6H_5)], has been previously computed and discussed. Indeed, the HOMO and HOMO-1, of similar energy, are π -type in character and result from antibonding interactions between the highest occupied π orbital of the sp carbon chain fragment and the filled $d-\pi$ orbitals of the two platinum fragments (Figure 5, top). This metal—carbon chain antibonding character is a common feature for carbon group containing organometallic species and governs their optical and/or redox properties. These HOMOs are mainly octatetraynediyl in character with a computed contribution close to 90%, whereas the platinum character is only ca. 10%. The LUMOs (Figure 5, top) are predominantly localized on the ancillary ligands attached to the metal centers with a weak metal participation (ca. 10%).

When 2 is threaded through the macrocycle to give 2·3, the HOMOs hardly change in character, but there is a slight energetic stabilization of ca. 0.25 eV due to electrostatic interactions with the macrocycle. The LUMOs of 2·3 are macrocycle-centered, located predominantly on the 1,10-phenanthroline moiety intercalating below the LUMOs of the Pt₂C₈ wire (Figure 5, bottom). Consequently, the HOMO–LUMO gap of the rotaxane is smaller than that computed for the components (Figure 4). It must be stressed that a very tiny charge transfer (0.015 e according to a Hirshfeld charge

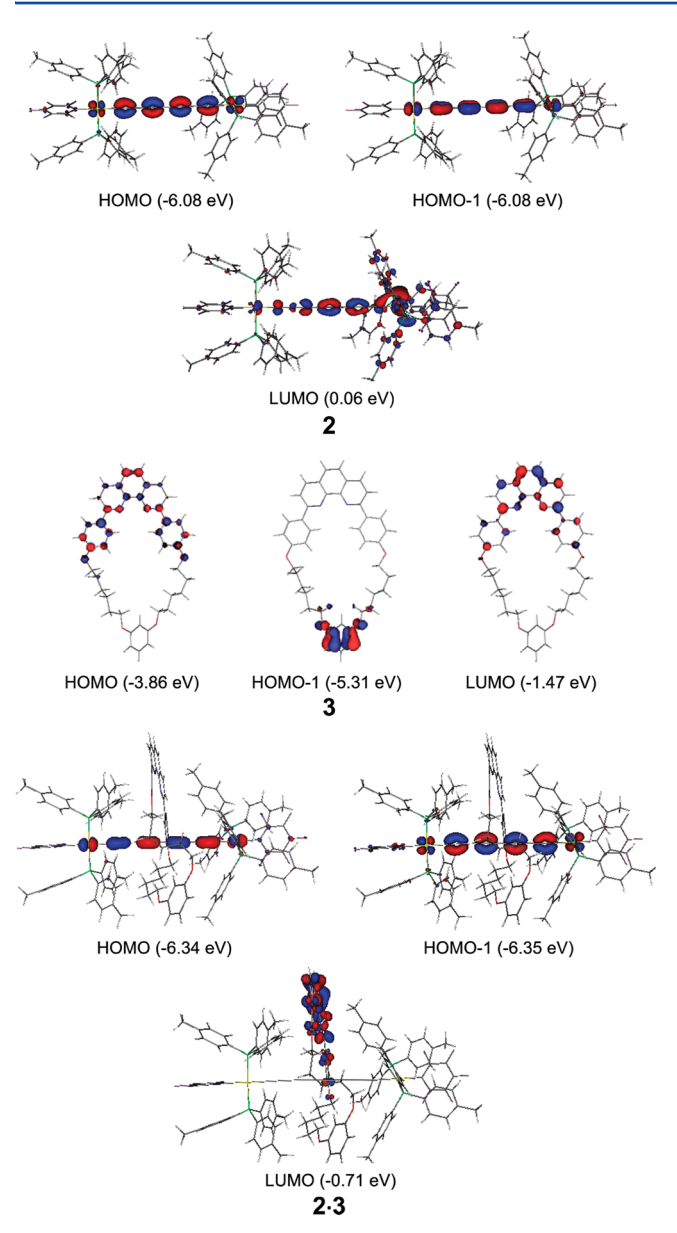


Figure 5. Plots of the HOMOs and LUMOs of $2\cdot3$ (bottom) and the components 2 (top) and 3 (middle). Contour values are ±0.03 (e/bohr³)^{1/2}. The energies are given in parentheses.

analysis¹⁶) occurs from the macrocycle to the axle upon threading.

3. UV-Vis Spectra. TD-DFT energies of the lowest allowed electronic excitations of the rotaxane and its components were computed. They are shown in Figure 6 and compared in Table 2. The agreement between the simulated and experimentally measured UV-vis spectra is reasonable. As observed experimentally, the computed UV-vis spectrum of 2.3 is essentially the sum of those of the Pt₂C₈ wire and the macrocycle, although some slight macrocycle to organometallic wire (or vice versa) charge transfer occurs according to the computed transitions responsible for the excitations. Most of the intense excitations of the former computed at (energy in nm, oscillator strength f in parentheses) 272 (1.32), 280 (0.08), 287 (0.29), and 297 (3.64) are found for the rotaxane at 279 (0.07), 287 (0.28), and 296 (3.32). A weak excitation computed for 2 at 420 (0.01) involving HOMO-LUMO region transitions, i.e., metal-ligand to ligand charge transfer, is also found for $2\cdot3$ at the same energy. The four intense excitations computed for the bead 3 at 281 (1.38), 287 (0.11), 321 (0.15), and 332 (0.70) are also found in the computed spectrum of the rotaxane $2\cdot3$ at similar energies and intensities (278 (1.10), 286 (0.11), 318 (0.11), and 326 (0.49)).

4. Oxidized Species. The redox properties of the rotaxane **2·3** have been experimentally studied and compared to those of the components **2** and **3.** Interestingly, cyclic voltammetry (CV) shows that the Pt_2C_8 wire **2** undergoes a quasi-reversible mono-oxidation at ca. 1.2 V (vs Ag/AgCl), whereas the macrocycle **3** undergoes irreversible oxidations at 1.40 and 1.71 V (no detectable anodic current). The rotaxane **2·3** also exhibits an irreversible oxidation, as evidenced by continually increasing cathodic current, with no "maxima" or other features, until the anodic scan is begun.

The adiabatic ionization potentials (IPs) were computed for the rotaxane and its components. For the wire 2, a value of 5.80 eV is found. A glance at the Hirshfeld¹⁶ atomic net charges of the neutral and cationic molecules (see Figure S1 (Supporting Information)) indicates that oxidation takes place mostly on the sp carbon chain. This is confirmed by the Hirshfeld¹⁶ atomic spin density computed for 2+, which is largely distributed over all of the carbon chain (Figure S2 (Supporting Information)). Geometry optimization of 2⁺ shows a shortening of the Pt-C and C-C single bonds by roughly 0.04 and 0.03 Å, respectively, and a slight elongation of the C≡C triple bonds by ca. 0.02 Å (Table 1). This is consistent with the nodal properties of the HOMO and HOMO-1 of 2 (vide supra). Depopulation of the metal-carbon slightly antibonding HOMOs is a common feature in organometallic wires. 1k The first and second IPs for the macrocycle 3 are 6.89 and 8.53 eV, respectively. These values are in agreement with the CV experiments, which show that the wire is more readily oxidized than the macrocycle. Interestingly, the first IP calculated for the rotaxane is 6.02 eV, slightly higher than that computed for the unthreaded organometallic wire. The oxidation of rotaxane 2.3 is therefore expected to be thermodynamically less favorable than that of the unwrapped wire.

5. Higher Homologues. So far, 2.3 is the only rotaxane containing a conjugated Pt_2C_n (n = 8) polyynediyl axle that has been structurally characterized. Higher homologues should be readily accessible, as oxidative homocouplings become more facile as the sp carbon chain is lengthened, and end group/ macrocycle steric interactions should diminish. As noted above, related rotaxanes featuring "organic" polyynes with 8, 12, and 20 sp carbon atoms in the axle and bulky tris(3,5-di-tertbutylphenyl)methyl end groups have been reported. 10 Thus, higher homologues of rotaxane 2.3 (R8) with 10 (R10), 12 (R12), and 14 (R14) sp carbon atoms were computed and analyzed. As expected, the Pt-C and C-C distances in the Pt₂C_n axles are similar overall (see Table S4 (Supporting Information)) and comparable to those measured for the unthreaded wires. 13 The HOMO-LUMO gaps—5.70, 5.47, and 5.26 eV for R10, R12, and R14, respectively—are comparable to that computed for 2.3 (R8) and monotonically decrease as with the unthreaded wires. 14 As for 2.3 (R8), very weak charge transfers occur from the macrocycle to the axle upon threading (0.031, 0.029, and 0.023 e according to a Hirshfeld¹⁶ charge analysis for R10, R12 and R14, respectively).

Geometry optimization indicates that, for R10 and R12, the polyme chain accommodates the macrocycle in its middle

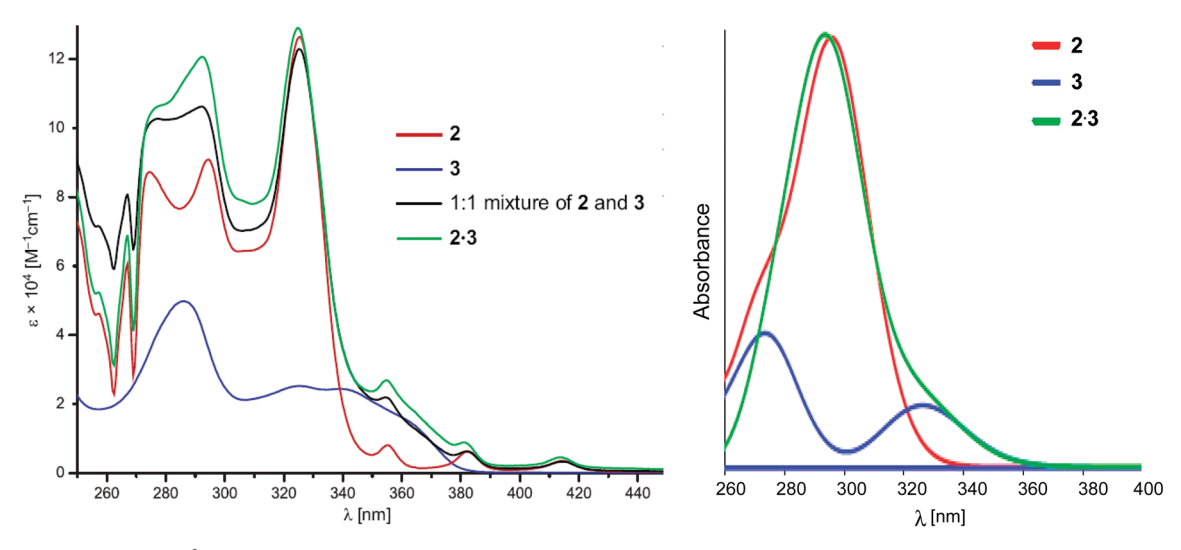


Figure 6. Experimental (left)⁹ and calculated (right) UV-vis spectra of 2·3 and the components.

(Figure 7), as observed for 2.3 and the structurally characterized "organic" C_{12} sp carbon chain containing rotaxane. ¹⁰ In the case of 2.3, the van der Waals contacts do not allow any appreciable slippage from the midpoint of the carbon chain, but R10 and R12 are less constrained. Interestingly, with R14, a substantial displacement of the macrocycle from the middle toward one platinum center is computed (Figure 7, bottom right).

The adiabatic noncovalent interaction energies between the thread and bead components of rotaxanes 2.3 (R8), R10, R12, and R14 were calculated using the long-range-separated CAM-B3LYP functional in order to understand the effect of the extension of the carbon chain. Interestingly, the binding energies decrease from R8 to R10 to R12 but increase again for R14, as depicted graphically in Figure 8 (exact values -13.27, -11.41, -7.71, and -8.15 kcal/mol). Computations on the "organic" polyyne rotaxanes, designated R8'-R14', exhibit the same trend but with binding energies 1 order of magnitude smaller, as also shown in Figure 8. Here, energies for the R8' and R10' analogues are attractive (-0.46 and -0.31 kcal/mol), but those for R12' and R14' are slightly repulsive (+0.63 and +0.06 kcal/mol). Importantly, when BSSE corrections are not taken into account, somewhat attractive energies are computed for R12' and R14' (-2.38 and -3.48 kcal/mol).

The shortest atomic contacts between the two components in the preceding rotaxanes were identified and are summarized in Table 3. The data indicate that the attractive interactions are mainly due to hydrogen bonds in the 2.50–3.10 Å range, as opposed to contacts involving atoms of the sp carbon chain (Table S3 (Supporting Information)). These involve the nitrogen and oxygen atoms of the macrocycle and both the C_6H_4 and CH_3 hydrogen atoms of the tolyl groups of the bulky phosphine ligands for the organometallic series R8-R14 or the CH_3 hydrogen atoms of the bulky tris(3,5-di-tert-butylphenyl)methyl end groups for the organic series R8'-R14'.

As shown in Table 3, the hydrogen bonds become longer and less numerous upon going from *R8* to *R12*, consistent with decreasing steric constraints on the macrocycle by the end groups. With *R12*, a slight S-shaped distortion of the carbon chain and a skewed threading of the macrocycle is evident (Figure 7). This facilitates synergistic hydrogen bonding involving both end groups, with N1 associated with the tolyl

hydrogen atoms of one platinum moiety and O2 and O3 associated with tolyl hydrogen atoms of the other.

Further lengthening of the carbon chain increases the translational freedom for "slippage" of the macrocycle within the rotaxane. Indeed, with R14, a displacement of the macrocycle toward one end group is computed, allowing shorter hydrogen contacts in comparison to R12 and thereby increasing the binding energy. To help interpret these data, an isomeric structure, $R14_{sym}$, was investigated (see Figure S3 (Supporting Information)). Here, the atoms of the macrocycle closest to the axle were restricted to the middle of the chain. Although conformational distortions allowed a single hydrogen bond to be maintained ($O2 \cdot \cdot \cdot H = 2.599 \text{ Å}$), the binding energy decreased (-6.15 vs -8.15 kcal/mol), as would be intuitively expected.¹⁷ Furthermore, these data explain why the "organic" polyyne rotaxanes R8'-R14', in which there are fewer and/or much longer heteroatom...H contacts (Table 3), exhibit much weaker binding energies (Figure 8).

CONCLUSION

The preceding DFT calculations have established that the electronic properties of rotaxanes generated by threading phosphine-substituted diplatinum polyynediyl complexes through a 1,10-phenanthroline-based macrocycle essentially correspond to those of the components. The bond distances and bond angles are also largely unperturbed. However, various types of hydrogen-bonding contacts involving the nitrogen and oxygen atoms of the macrocycle and p-tolyl hydrogen atoms of the phosphine ligands are identified. These are maximized at shorter sp carbon chain lengths, which position the macrocycle and platinum phosphine end groups at van der Waals distances. However, some contacts are maintained at longer chain lengths, by either skewing of the macrocycle or slippage toward one end group. All of these motifs provide a much greater contribution to the interaction energies than the weak van der Waals attractions derived from the close proximity of the sp carbon chain to the macrocycle atoms and other van der Waals contacts enforced by the mechanical bond. This is further evidenced by the much weaker interaction energies in related rotaxanes that feature organic polyynes with bulky triarylmethane end groups that are apparently much less disposed to hydrogen bonding.

Table 2. Computed Energies (λ, nm) , Oscillator Strengths (f), Main Composition, and Main Assignment of the First UV–Vis Electronic Excitations for 2, 3 and 2·3

λ (f)	main composition	main assignment	
	Compound 2		
269 (0.02)	58% HOMO → LUMO+2	$PtC_8Pt \rightarrow p-tol_3P$	
	13% HOMO-5 → LUMO+2	$(PtC_8Pt)C_6F_5 \rightarrow p-tol_3P$	
272 (1.32)	11% HOMO-14 \rightarrow LUMO+1	$PtC_8Pt \rightarrow p-tol_3P$	
	7% HOMO → LUMO+1	$PtC_8Pt \rightarrow p-tol_3P$	
280 (0.08)	47% HOMO-1 → LUMO+2	$PtC_8Pt \rightarrow p-tol_3P$	
287 (0.29)	14% HOMO-15 → LUMO	$PtC_8Pt \rightarrow C_8$ (carbon chain)	
	8% HOMO-4 → LUMO		
297 (3.64)	25% HOMO → LUMO+1	$PtC_8Pt \rightarrow p-tol_3P$	
	22% HOMO-1 → LUMO	$PtC_8Pt \rightarrow C_8$ (carbon chain)	
420 (0.01)	35% HOMO-1 → LUMO	$PtC_8Pt \rightarrow C_8$ (carbon chain)	
	31% HOMO → LUMO+1	$PtC_8Pt \rightarrow p-tol_3P$	
	Compound 3	-	
281 (1.38)	56% HOMO-2 → LUMO	$L1^a \rightarrow L1$	
	20% HOMO → LUMO+2	$L1 \rightarrow L1$	
287 (0.11)	70% HOMO-2 \rightarrow LUMO+1	$L1 \rightarrow L1'$	
321 (0.15)	60% HOMO → LUMO+1	$L1 \rightarrow L1'$	
	21% HOMO-2 → LUMO	$L1 \rightarrow L1$	
332 (0.70)	87% HOMO → LUMO	$L1 \rightarrow L1$	
	7% HOMO-2 → LUMO+2	$L1 \rightarrow L1$	
	Compound 2·3		
278 (1.10)	54% HOMO-4 → LUMO	macrocycle → macrocycle	
	14% HOMO-2 → LUMO+7	macrocycle → macrocycle	
279 (0.07)	12% HOMO-19 → LUMO+1	$PtC_8Pt \rightarrow macrocycle$	
, ,	8% HOMO-21 → LUMO+3	$PtC_8Pt (p-tol_3P) \rightarrow PtC_8Pt$	
286 (0.11)	66% HOMO-4 → LUMO+2	$macrocycle \rightarrow PtC_8Pt$	
287 (0.28)	12% HOMO-21 → LUMO+1	$PtC_8Pt (p-tol_3P) \rightarrow macrocycle$	
	8% HOMO-19 → LUMO+3	$PtC_8Pt \rightarrow PtC_8Pt$	
296 (3.32)	18% HOMO-1 → LUMO+3	$PtC_8Pt \rightarrow PtC_8Pt$	
	17% HOMO → LUMO+3	$PtC_8Pt \rightarrow PtC_8Pt$	
	15% HOMO-1 → LUMO+1	$PtC_8Pt \rightarrow macrocycle$	
	15% HOMO → LUMO+1	PtC ₈ Pt → macrocycle	
318 (0.11)	55% HOMO-2 → LUMO+2	$macrocycle \rightarrow PtC_8Pt$	
	20% HOMO-4 → LUMO	macrocycle → macrocycle	
326 (0.49)	82% HOMO-2 → LUMO	macrocycle → macrocycle	
420 (0.01)	25% HOMO-1 → LUMO+1	PtC ₈ Pt → macrocycle	
	23% HOMO → LUMO+1	PtC ₈ Pt → macrocycle	
	21% HOMO → LUMO+3	$PtC_8Pt \rightarrow C_8 \ (carbon \ chain)$	
	21% HOMO-1 → LUMO+3	$PtC_8Pt \rightarrow C_8$ (carbon chain)	

^aL1: (2,9-(1,10-phenanthrolinediyl)(p-C₆H₄O)₂ fragment. L1': 1,10-phenanthroline fragment.

■ EXPERIMENTAL SECTION

1. Computational Details. Density functional theory (DFT) calculations were performed using the Gaussian09 program package. Full geometry optimizations were carried out on both neutral and monocationic systems without any symmetry constraint using the CAM-B3LYP functional¹⁹ within the LANL2DZ ECP basis set which partially takes into account the relativistic effects on Pt, 20 augmented by a polarization function for all atoms except H. Time-dependent density functional theory (TD-DFT) calculations were performed on the optimized structures of 2.3 and its components using the CAM-B3LYP functional, taking into account the solvation effects of the dichloromethane solvent using the PCM model.²¹ The noncovalent interaction energies between the axle and the bead were corrected for the basis set superposition error (BSSE) using the counterpoise correction.²² Molecular structures and orbitals were plotted using the Molekel program. 23 Orbital compositions were obtained using the AOMix program.²⁴ The UV-vis spectra have been simulated from the computed TD-DFT transitions by using the SWizard program,²⁵ each transition being associated with a Gaussian function of half-height width equal to 3000 cm⁻¹.

2. Crystallography. A CH₂Cl₂ solution of 3²⁶ was allowed to slowly evaporate at room temperature. After 3 days, colorless plateshaped crystals were analyzed as summarized in Table S1 (Supporting Information). Cell parameters were obtained from 1080 frames using a 0.5° scan using Cell_Now²⁷ and refined with 24948 reflections. Integrated intensity information for each reflection was obtained by reduction of the data frames with APEX2.²⁸ The integration method employed a three-dimensional profiling algorithm, and all data were corrected for Lorentz and polarization factors, as well as for crystal decay effects. The data were merged and scaled to produce a suitable data set, which was corrected for absorption effects using SADABS.²⁹ Systematic reflection conditions and statistical tests indicated the space group (Pn), and the structure was solved using SHELXTL (SHELXS).³⁰ Hydrogen atoms were placed in idealized positions and were refined using a riding model. All non-hydrogen atoms were refined with anisotropic thermal parameters. The structure was refined (weighted least-squares refinement on F^2) to convergence.³⁰

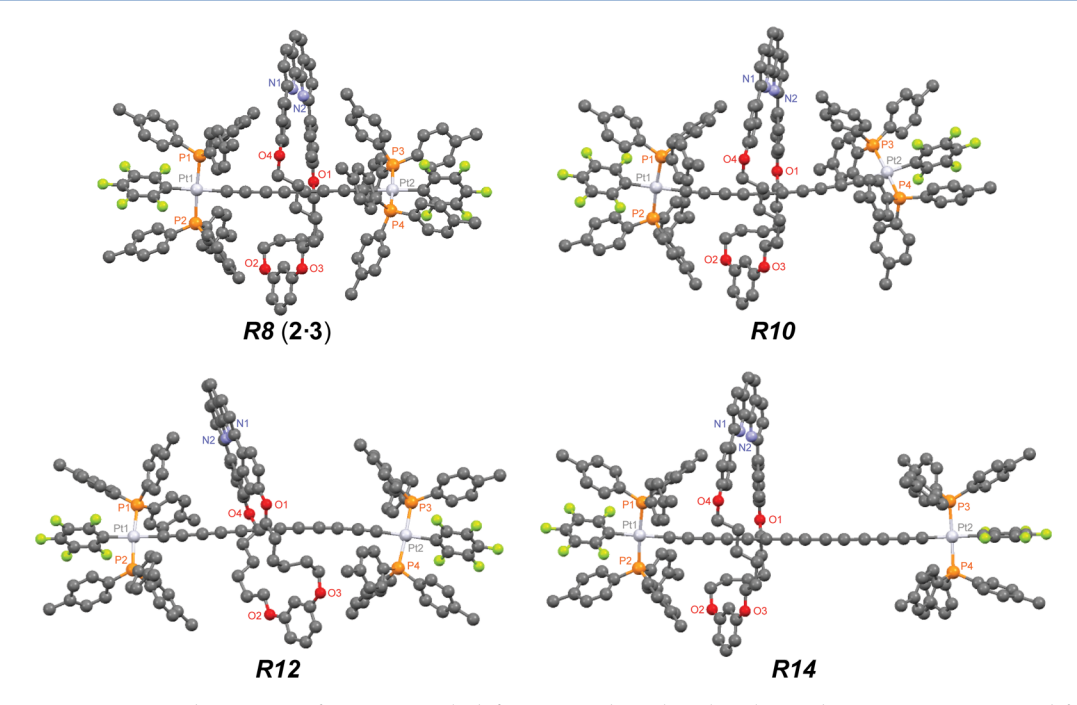


Figure 7. Lowest energy optimized structures of rotaxanes with different sp carbon chain lengths. Hydrogen atoms are omitted for clarity.

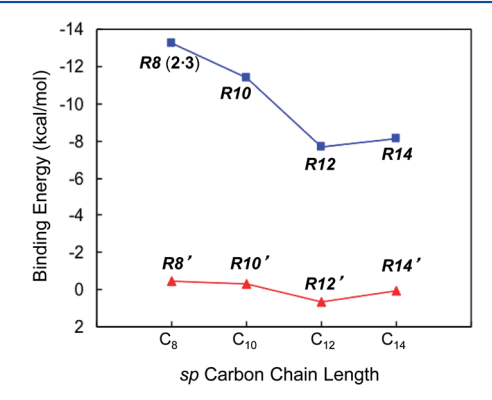


Figure 8. Binding energies (BE, kcal/mol) in organometallic (\blacksquare) and organic (\triangle) rotaxanes.

Table 3. Shortest Hydrogen Bonding Contacts (Å) between the Axle and the Bead for Organometallic and Organic Rotaxanes a

	organometallic rotaxane				
	R8 (2·3)	R10	R12	R14 ^b	
$N1\cdots H(C_{sp^3})$	3.001	2.806	2.951	2.666	
$N1\cdots H(C_{sp}^{-2})$	2.868				
$N2\cdots H(C_{sp}^{3})$	2.661	2.749			
$N2\cdots H(C_{sp}^{2})$	3.049	2.867			
$O1 \cdots H(C_{sp}^{3})$	2.683	2.631			
$O2\cdots H(C_{sp}^3)$	2.534	2.581	2.774	2.578	
$O3\cdots H(C_{sp}^{3})$	2.700				
$O4\cdots H(C_{sp}^{2})$	3.114	3.156	2.794		
•	organic rotaxane				
	R8'	R10′	R12′	R14′	
$N2\cdots H(C_{sp^3})$	3.287	3.130		2.902	
$O1\cdots H(C_{m}^{1})$	2.849	3.019		2.892	

 a H(C_{sp}^{3}) refers to a CH₃ proton of the axle end group and H(C_{sp}^{2}) to a C_{6} H₄ proton. b Only one short H bonding contact is computed for $R14_{sym}$ (O2···H = 2.599 Å).

ASSOCIATED CONTENT

S Supporting Information

Text, figures, tables, and a CIF file giving the optimized procedure for the synthesis of 3, Hirshfeld atomic net charges for neutral 2 and cationic 2⁺, Hirshfeld atomic spin density for 2^+ , optimized structure of rotaxane $R14_{sym}$, crystal and structure refinement data for 3, computed and crystallographic bond lengths for the macrocycle in 3 and 2.3, stacking and axle/ macrocycle contacts in 2.3, selected computed bond lengths for homologues of 2.3 with longer axles, Cartesian coordinates for all calculated geometries, and a CIF file giving crystallographic data for 3. This material is available free of charge via the Internet at http://pubs.acs.org. Full details of the structure determination have also been deposited with the Cambridge Crystallographic Data Centre as CCDC 950619. Copies of this information may be obtained free of charge from The Director, CCDC, 12 Union Street, Cambridge CB2 1EZ, U.K. (fax, +44-1223-336-033; e-mail, deposit@ccdc.cam.ac.uk).

AUTHOR INFORMATION

Corresponding Authors

*E-mail for J.A.G.: gladysz@mail.chem.tamu.edu.

*E-mail for J.-F.H.: halet@univ-rennes1.fr.

Author Contributions

The manuscript was written through contributions of all authors. All authors have given approval to the final version of the manuscript.

Notes

The authors declare no competing financial interest.

ACKNOWLEDGMENTS

We thank the PROFAS French-Algerian Program for a Ph.D. Fellowship (H.S.) and the US National Science Foundation (CHE-1153085) for support (Z.B., J.A.G.).

d. det een (10 1001 (een 100700 - 1 0een een skellter 2012 | 22 | 6260 | 6267

REFERENCES

- (1) See for example: (a) Lang, H. Angew. Chem., Int. Ed. Engl. 1994, 33, 547-550; Angew. Chem. 1994, 106, 569-572. (b) Paul, F.; Lapinte, C. Coord. Chem. Rev. 1998, 178-180, 427-505. (c) Paul, F.; Lapinte, C. In Unusual Structures and Physical Properties in Organometallic Chemistry; Gielen, M., Willem, R., Wrackmeyer, B., Eds.; Wiley: London, 2002; pp 220-291. (d) Szafert, S.; Gladysz, J. A. Chem. Rev. 2003, 103, 4175-4206; Chem. Rev. 2006, 106, PR1-PR33. (e) Long, N. J.; Williams, C. K. Angew. Chem., Int. Ed. 2003, 42, 2586-2617; Angew. Chem. 2003, 115, 2690-2722. (f) Bruce, M. I.; Low, P. J. Adv. Organomet. Chem. 2004, 50, 179-444. (g) Bruce, M. I. Coord. Chem. Rev. 2004, 248, 1603-1625. (h) Ren, T. Organometallics 2005, 24, 4854-4870. (i) Akita, M.; Koike, T. Dalton Trans. 2008, 3523-3530. (j) Low, P. J. Coord. Chem. Rev. 2013, 257, 1507-1532. (k) Halet, J.-F.; Lapinte, C. Coord. Chem. Rev. 2013, 257, 1584-1613. (2) Lehn, J.-M. Supramolecular Chemistry; VCH: Weinheim, Germany, 1995.
- (3) (a) Low, P. J. Dalton Trans. 2005, 2821–2824. (b) Tao, N. J. Nat. Nanotechnol. 2006, 1, 173–181.
- (4) See for example: (a) Bartik, T.; Bartik, B.; Brady, M.; Dembinski, R.; Gladysz, J. A. Angew. Chem., Int. Ed. Engl. 1996, 35, 414–417; Angew. Chem. 1996, 108, 467–469. (b) Sakurai, A.; Akita, M.; Morooka, Y. Organometallics 1999, 18, 3241–3244. (c) Rigaut, S.; Perruchon, J.; Le Pichon, L.; Touchard, D.; Dixneuf, P. H. J. Organomet. Chem. 2003, 670, 37–44. (d) Xu, G.-L.; Zou, G.; Ni, Y.-H.; DeRosa, M. C.; Crutchley, R. J.; Ren, T. J. Am. Chem. Soc. 2003, 125, 10057–10065. (e) Antonova, A. B.; Bruce, M. I.; Ellis, B. G.; Gaudio, M.; Humphrey, P. A.; Jevric, M.; Melino, G.; Nicholson, B. K.; Perkins, G. J.; Skelton, B. W.; Stapleton, B.; White, A. H.; Zaitseva, N. N. Chem. Commun. 2004, 960–961. (f) Qi, H.; Gupta, A.; Noll, B. C.; Snider, G. L.; Lu, Y.; Lent, C.; Fehlner, T. P. J. Am. Chem. Soc. 2005, 127, 15218–15227.
- (5) See for example: (a) Bruce, M. I.; Costuas, K.; Gendron, F.; Halet, J.-F.; Jevric, M.; Skelton, B. W. *Organometallics* **2012**, *31*, 6555–6566. (b) Burgun, A.; Gendron, F.; Roisnel, T.; Sinbandhit, S.; Costuas, K.; Halet, J.-F.; Bruce, M. I.; Lapinte, C. *Organometallics* **2013**, *32*, 1866–1875.
- (6) See for instance: Bruce, M. I.; Le Guennic, B.; Scoleri, N.; Zaitseva, N. N.; Halet, J.-F. *Organometallics* **2012**, *31*, 4701–4706 and references therein.
- (7) Frampton, M. J.; Anderson, H. L. Angew. Chem., Int. Ed. 2007, 46, 1028–1064; Angew. Chem. 2007, 119, 1046–1083.
- (8) (a) Stahl, J.; Bohling, J. C.; Bauer, E. B.; Peters, T. B.; Mohr, W.; Martín-Alvarez, J. M.; Hampel, F.; Gladysz, J. A. Angew. Chem., Int. Ed. 2002, 41, 1871–1876; Angew. Chem. 2002, 114, 1951–1957. (b) Stahl, J.; Mohr, W.; de Quadras, L.; Peters, T. B.; Bohling, J. C.; Martín-Alvarez, J. M.; Owen, G. R.; Hampel, F.; Gladysz, J. A. J. Am. Chem. Soc. 2007, 129, 8282–8295. (c) de Quadras, L.; Bauer, E. B.; Mohr, W.; Bohling, J. C.; Peters, T. B.; Martín-Alvarez, J. M.; Hampel, F.; Gladysz, J. A. J. Am. Chem. Soc. 2007, 129, 8296–8309. (d) de Quadras, L.; Bauer, E. B.; Stahl, J.; Zhuravlev, F.; Hampel, F.; Gladysz, J. A. New J. Chem. 2007, 31, 1594–1604. (e) Owen, G. R.; Stahl, J.; Hampel, F.; Gladysz, J. A. Chem. Eur. J. 2008, 14, 73–87.
- (9) Weisbach, N.; Baranová, Z.; Gauthier, S.; Reibenspies, J. H.; Gladysz, J. A. Chem. Commun. 2012, 48, 7562–7564.
- (10) Movsisyan, L. D.; Kondratuk, D. V.; Franz, M.; Thompson, A. L.; Tykwinski, R. R.; Anderson, H. L. Org. Lett. 2012, 14, 3424–3426.
- (11) (a) Stoddart, J. F. Chem. Soc. Rev. 2009, 38, 1802–1820.
 (b) Bruns, C. J.; Stoddart, J. F. Top. Curr. Chem. 2012, 323, 19–72.
- (12) Waller, M. P.; Kruse, H.; Mück-Lichtenfeld, C.; Grimme, S. Chem. Soc. Rev. 2012, 41, 3119–3128.
- (13) (a) Mohr, W.; Stahl, J.; Hampel, F.; Gladysz, J. A. *Inorg. Chem.* **2001**, 40, 3263–3264. (b) Mohr, W.; Stahl, J.; Hampel, F.; Gladysz, J. A. *Chem. Eur. J.* **2003**, 9, 3324–3340.
- (14) Zhuravlev, F.; Gladysz, J. A. Chem. Eur. J. 2004, 10, 6510-6522.
- (15) See for example: (a) Bruce, M. I.; Low, P. J.; Costuas, K.; Halet, J.-F.; Best, S. P.; Heath, G. A. J. Am. Chem. Soc. **2000**, 122, 1949–1962. (b) Coat, F.; Paul, F.; Lapinte, C.; Toupet, L.; Costuas, K.; Halet, J.-F. J. Organomet. Chem. **2003**, 683, 368–378.

- (16) Hirshfeld, F. L. Theor. Chim. Acta 1977, 44, 129-138.
- (17) As found with R12, the sp carbon chain of $R14_{sym}$ is computed to be S-shaped, with some bending of the macrocycle (Figure S3 (Supporting Information)).
- (18) Frisch, M. J.; Trucks, G. W.; Schlegel, H. B.; Scuseria, G. E.; Robb, M. A.; Cheeseman, J. R.; Scalmani, G.; Barone, V.; Mennucci, B.; Petersson, G. A.; Nakatsuji, H.; Caricato, M.; Li, X. Hratchian, H. P.; Izmaylov, A. F.; Bloino, J.; Zheng, G.; Sonnenberg, J. L.; Hada, M.; Ehara, M.; Toyota, K.; Fukuda, R.; Hasegawa, J.; Ishida, M.; Nakajima, T.; Honda, Y.; Kitao, O.; Nakai, H.; Vreven, T.; Montgomery, J. A., Jr..; Peralta, J. E.; Ogliaro, F.; Bearpark, M.; Heyd, J. J.; Brothers, E.; Kudin, K. N.; Staroverov, V. N.; Keith, T.; Kobayashi, R.; Normand, J.; Raghavachari, K.; Rendell, A.; Burant, J. C.; Iyengar, S. S.; Tomasi, J.; Cossi, M.; Rega, N.; Millam, J. M.; Klene, M.; Knox, J. E.; Cross, J. B.; Bakken, V.; Adamo, C.; Jaramillo, J.; Gomperts, R.; Stratmann, R. E.; Yazyev, O.; Austin, A. J.; Cammi, R.; Pomelli, C.; Ochterski, J. W.; Martin, R. L.; Morokuma, K.; Zakrzewski, V. G.; Voth, G. A.; Salvador, P.; Dannenberg, J. J.; Dapprich, S.; Daniels, A. D.; Farkas, O.; Foresman, J. B.; Ortiz, J. V.; Cioslowski, J.; Fox, D. J. Gaussian 09, Revision A.02; Gaussian, Inc., Wallingford, CT, 2009.
- (19) Yanai, T.; Tew, D. P.; Handy, N. C. Chem. Phys. Lett. **2004**, 393, 51–57.
- (20) (a) Dunning, T. H. Jr.; Hay, P. J. Modern Theoretical Chemistry; Plenum: New York, 1976; Vol. 3, pp 1–28. (b) Hay, P. J.; Wadt, W. R. J. Chem. Phys. 1985, 82, 270–283; J. Chem. Phys. 1985, 82, 284–298; J. Chem. Phys. 1985, 82, 299–310.
- (21) Tomasi, J.; Mennucci, B.; Cammi, R. Chem. Rev. 2005, 105, 2999–3093.
- (22) (a) Boys, S. F.; Bernardi, F. Mol. Phys. 1970, 19, 553–566. (b) Simon, S.; Duran, M.; Dannenberg, J. J. J. Chem. Phys. 1996, 105, 11024–11031.
- (23) (a) Flükiger, P.; Lüthi, H. P.; Portmann, S.; Weber, J. *MOLEKEL 4.3*; Swiss Center for Scientific Computing, Manno, Switzerland, 2000–2002. (b) Portmann, S.; Lüthi, H. P. *Chimia* **2000**, 54, 766–770.
- (24) (a) Gorelsky, S. I. AOMix: Program for Molecular Orbital Analysis; University of Ottawa, Ottawa, Canada, 2007; http://www.sg-chem.net. (b) Gorelsky, S. I.; Lever, A. B. P. J. Organomet. Chem. 2001, 635, 187–196.
- (25) Gorelsky, S. I. SWizard Program; University of Ottawa, Ottawa, Canada, 2007; http://www.sg-chem.net.
- (26) Saito, S.; Nakazono, K.; Takahashi, E. J. Org. Chem. 2006, 71, 7477–7480.
- (27) Sheldrick, G. M. Cell_Now (version 2008/1): Program for Obtaining Unit Cell Constants from Single Crystal Data; University of Göttingen, Göttingen, Germany, 2008.
- (28) APEX2: Program for Data Collection and Integration on Area Detectors; Bruker AXS Inc., 5465 East Cheryl Parkway, Madison, WI 53711-5373 USA.
- (29) Sheldrick, G. M. SADABS (version 2008/1): Program for Absorption Correction for Data from Area Detector Frames; University of Göttingen, Göttingen, Germany, 2008.

(30) Sheldrick, G. M. Acta Crystallogr. 2008, A64, 112-122.